

Cracking the olivine zoning code: distinguishing between crystal growth and diffusion

By Thomas Shea, Kendra J. Lynn and Michael O. Garcia

METHODS 1: EPMA ANALYSES

The University of Hawaii JEOL 8500F Hyperprobe Field-Gun Emission microprobe was used to analyze olivine, as well as glass in the surrounding matrix and in a melt inclusion.

Spot analyses and transects in olivine

High precision olivine analyses were conducted using an accelerating voltage of 20 keV, a current of 200 nA, and a beam diameter of 6 μm for spot measurements in the selected olivine to provide anchor points to calibrate x-ray maps (see below). For the two transects, the beam diameter was set at 2 μm to ensure high spatial resolution and to minimize analytical overlap. Peak counting times were 80 s (Si, Fe, Mg, and Ni) and 30 s (Ca, note: only measured in transect 2) and background counting times were half as long. Standard olivines Springwater (Fo_{83}) and San Carlo (Fo_{90}) were analyzed repeatedly to check for analytical drift. Relative analytical precision based on two standard deviations of standard analyses is $<0.5\%$ for Si, Fe, Mg, and around 1.5% for Ni and Ca. Data for one of the transects (T2) is reported below (Table DR1).

Spot analyses in the groundmass glass and melt inclusion

For glass analyses, an accelerating voltage of 15 keV, a current of 10 nA, a beam diameter of 10 μm , with on-peak counting times of 30 s (Si, Ti, Fe, Mn, Na, K, P, S, Cl) and 70 s (Al, Mg, Ca) were used. Time-Dependent Intensities (TDI) were measured every 5 s to check for any Si, Ti, Na, K, P changes during the analysis. Within uncertainty, no TDI were detected for Si, Ti, K and P, and TDI losses in Na were of $\leq 1\%$ relative. Smithsonian glasses VG-2 and A99 were used for Si, Al, Mg, Ca, and Fe (Jarosewich et al. 1980). Other elements were analyzed with well-known mineral standards (Verma Garnet for Mn, Amelia Albite for Na, OR-1 Orthoclase for K, USNM 104021 F-Apatite for Cl, and Staunton Meteorite for S). Analytical precision based on two

standard deviations of standard material analyses is about 1% (Si, Al, Mg, Ca) 3-5% (Fe, K, Na) 15-25% (Ti, Mn, S, Cl), and 30% (P) relative. Analytical results are reported in Table DR2.

Table DR1: Transect T2 EMP analyses in the Kilauea olivine.

	SiO ₂ (wt.%)	FeO	NiO	MgO	CaO	% Fo	distance (μm)
kil_skel_ol_tr2_1	40.92	13.08	0.335	46.59	0.200	86.39	0
kil_skel_ol_tr2_2	40.93	13.12	0.333	46.57	0.190	86.36	8
kil_skel_ol_tr2_3	40.98	13.14	0.333	46.52	0.207	86.33	16
kil_skel_ol_tr2_4	41.04	13.22	0.333	46.56	0.196	86.26	25
kil_skel_ol_tr2_5	41.07	13.32	0.330	46.56	0.194	86.17	33
kil_skel_ol_tr2_6	41.00	13.29	0.327	46.40	0.205	86.15	41
kil_skel_ol_tr2_7	40.90	13.39	0.327	46.39	0.202	86.07	49
kil_skel_ol_tr2_8	40.97	13.50	0.326	46.31	0.189	85.95	57
kil_skel_ol_tr2_9	41.01	13.61	0.326	46.20	0.202	85.82	65
kil_skel_ol_tr2_10	41.04	13.74	0.321	46.09	0.201	85.67	74
kil_skel_ol_tr2_11	41.04	13.90	0.321	45.95	0.196	85.50	82
kil_skel_ol_tr2_12	40.95	14.07	0.311	45.78	0.206	85.29	90
kil_skel_ol_tr2_13	40.92	14.26	0.308	45.63	0.197	85.08	98
kil_skel_ol_tr2_14	40.90	14.45	0.301	45.43	0.205	84.86	106
kil_skel_ol_tr2_15	40.90	14.69	0.307	45.21	0.205	84.59	114
kil_skel_ol_tr2_16	40.85	14.89	0.294	44.96	0.193	84.33	123
kil_skel_ol_tr2_17	40.81	15.24	0.290	44.79	0.198	83.98	131
kil_skel_ol_tr2_18	40.75	15.45	0.286	44.52	0.210	83.70	139
kil_skel_ol_tr2_19	40.69	15.74	0.276	44.26	0.201	83.36	147
kil_skel_ol_tr2_20	40.58	16.09	0.272	44.07	0.214	83.00	155
kil_skel_ol_tr2_21	40.40	16.38	0.268	43.79	0.217	82.65	163
kil_skel_ol_tr2_22	40.28	16.69	0.255	43.64	0.222	82.34	172
kil_skel_ol_tr2_23	40.23	16.93	0.251	43.29	0.242	82.01	180
kil_skel_ol_tr2_24	39.89	18.55	0.227	41.68	0.346	80.02	188

Table DR2: EPM analyses of matrix glass and melt inclusion (n=number of analyses averaged).

	SiO ₂	TiO ₂	Al ₂ O ₃	FeO	MnO	MgO	CaO	Na ₂ O	K ₂ O	P ₂ O ₅	SO ₃
Mat. Glass (n=5)	49.45	3.03	13.22	12.5	0.16	6.19	11.15	3.26	0.58	0.30	0.00
2σ	0.74	0.26	0.10	0.25	0.03	0.10	0.12	0.32	0.06	0.08	0.01
Melt Inclusion (n=3)	51.69	2.42	14.52	8.81	0.11	6.11	12.86	2.14	0.51	0.24	0.25
2σ	0.33	0.22	0.10	0.24	0.02	0.27	0.21	0.36	0.02	0.06	0.05

X-ray intensity maps

Map analyses of Fe, Mg, Ni, P and Al were performed in the same olivine crystal. Fe and Mg are two major components that are usually used for diffusion studies, whereas Ni diffuses slightly slower (Costa et al. 2008). P and Al are known to diffuse very slowly and can mark the original growth sequence of an olivine (Milman-Barris et al. 2008; Welsch et al. 2013, 2014). The maps were acquired using an accelerating voltage of 20 keV and a current of 300 nA, on a 900×800

pixel area, with a 1.5 $\mu\text{m}/\text{pixel}$ resolution and a dwell time of 220 μs per pixel. The X-ray maps took 52 h to complete. The resulting maps were extracted as raw intensity data. The Fe and Mg intensity data was then calibrated using the high-precision spot and transect analyses to yield quantitative maps. The other maps (Ni, P, Al) were left as relative intensity data. The Ni and Al maps are reported below (Figure DR1).

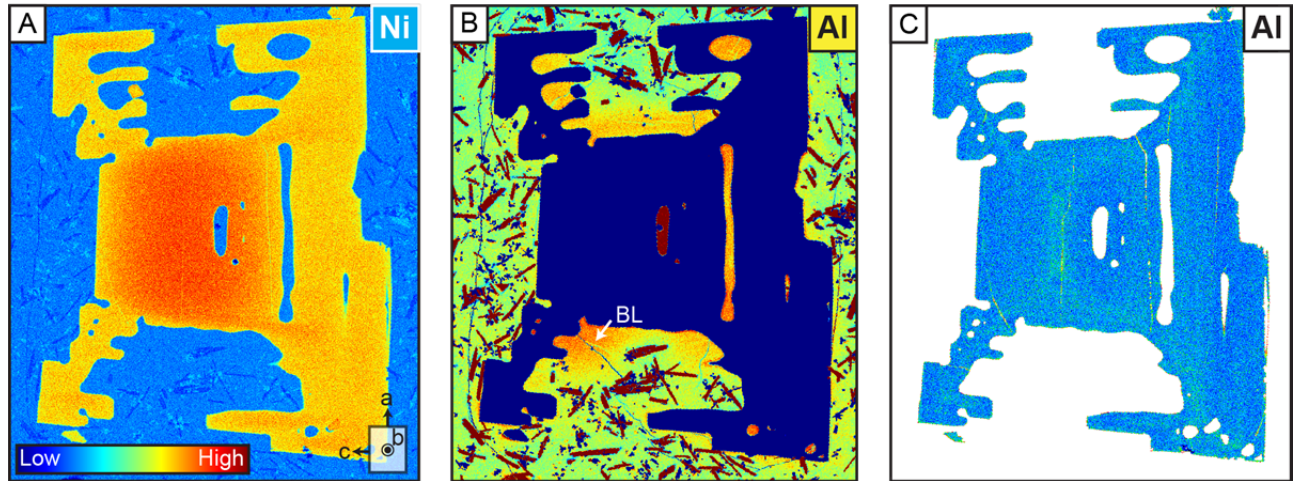


Figure DR1. Ni and Al intensity maps for the selected skeletal olivine. (A) Nickel displays zoning patterns similar to Fe-Mg, with two finger-shaped re-entrants towards the rim on the right (see main text). (B) Aluminum map with color scaling adjusted to resolve concentration differences in the groundmass glass. Note the boundary layer (BL) enriched in Al around the olivine, particularly within the partially closed hopper pockets and open melt inclusions. This boundary layer is presumably due to the last crystallization stage (ascent or quench rim, see Fig. 1 in the main text) and not the growth stage that formed the main skeletal branches. (C) Aluminum map with color scale adjusted to highlight the minute variations in the olivine. Zoning patterns are subtle but similar to those observed in the P map (Figure 1A).

METHODS 2: EBSD ANALYSIS

The orientation of the Kilauea olivine with respect to the thin section was obtained using Electron Backscatter Diffraction (EBSD) patterns on a JEOL 5900 Scanning Electron Microscope at the University of Hawaii. These patterns confirmed that the section was oriented nearly parallel to a-c, with a 9.5° inclination with respect to the b axis. This inclination was used to section the 3D models and compare the concentration gradients with the real 2D map (see below).

METHODS 3: DIFFUSION MODELS

Both the 2D and 3D diffusion models employed the concentration-dependent expression of Fick's 2nd law (one of the main directions being removed in the 2D model):

$$\frac{\partial C_i}{\partial t} = \left[\frac{\partial}{\partial x} \left(D_a \frac{\partial C_i}{\partial x} \right) + \frac{\partial}{\partial y} \left(D_b \frac{\partial C_i}{\partial y} \right) + \frac{\partial}{\partial z} \left(D_c \frac{\partial C_i}{\partial z} \right) \right]$$

Where C_i is the concentration of element i , D_a , D_b and D_c the diffusivities along the a , b and c crystallographic axes, and x , y and z the cartesian distance coordinates.

For Fe-Mg, the diffusivity along c is calculated using the expression of Dohmen et al. (2007):

$$D_c^{Fe-Mg} = 10^{-9.21} \left(\frac{fO_2}{10^{-7}} \right)^{\frac{1}{6}} 10^{3(0.9-X_{Fo})} \exp \left(- \frac{201000 + (P-10^5) \cdot 7 \times 10^{-6}}{RT} \right)$$

Where fO_2 is the oxygen fugacity in Pa, X_{Fo} the forsterite content of the olivine, P the pressure in Pa, R is the gas constant and T the temperature in K.

The models incorporate diffusion anisotropy using (Chakraborty 2010):

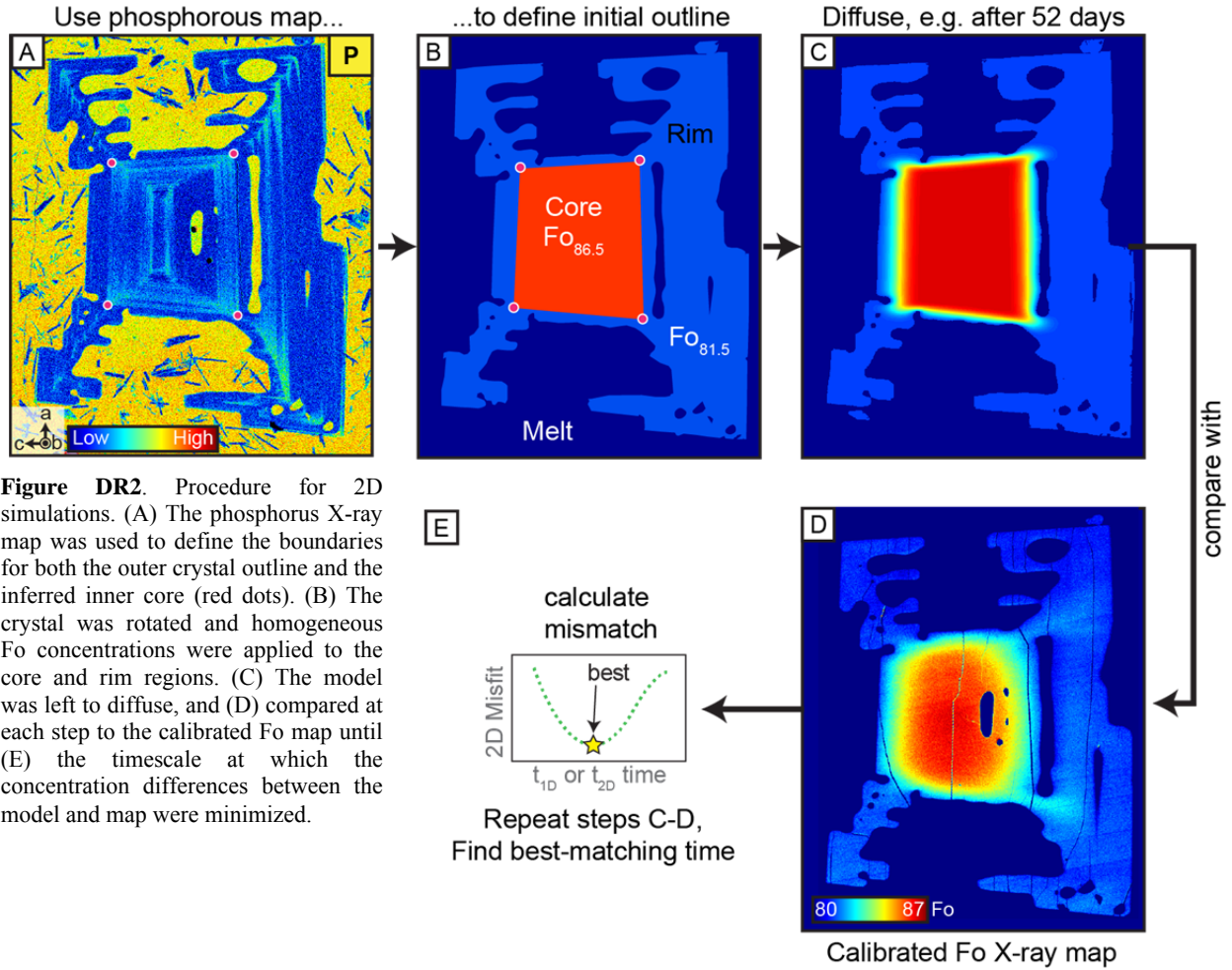
$$D_a = D_b = \frac{1}{6} D_c$$

After constructing the numerical olivines (see below), the 2D and 3D grids consisting of olivine and melt were used as inputs within finite difference implementations of the diffusion equations using Matlab[®]. Simplified 1D versions of the finite difference models were compared with 1D analytical solutions to ensure the validity of the approach.

2D Model

The advantage of this 2D model is that the crystal outline and diffusion grid were set to match the X-ray map and provided a direct means to compare goodness of fit. The disadvantage of the 2D model for complex skeletal morphologies is that diffusive fluxes from the third dimension (here, along the b -axis) are not considered (Shea et al., 2015). The initial crystal used for the 2D model was constructed by extracting outlines directly from the X-ray maps. The outer crystal outline was digitized following the glass-olivine boundary, and the initial undiffused higher Fo core was defined by the outline of the inner zones in the Phosphorus map (Figure DR2A and DR2B). In the model, the closed melt inclusions were ignored and filled in as being part of the high Fo core. The 2D initial olivine was then rotated for the Cartesian coordinates x and y to match the a and c crystallographic axes (Figure DR2B). Rotation and cropping resulted in an initial matrix of 780×630 pixels, which was used as the main input to the diffusion model, employing the same grid spacing as the x-ray map (1.5 μm/pixel). The models were run for diffusion timescales of 1.5 years, and after each increment of diffusion, the model was compared

with the calibrated Fo X-ray map (Figure DR2C to DR2D). The best matching timescale was obtained by minimizing the discrepancy between the model and map (Figure DR2E).



3D Model

The advantage of the 3D model is the ability to account for fluxes in all directions, incorporate potential morphological effects (e.g. merging diffusion fronts, Shea et al. 2015) and avoid the problems of sectioning. The drawback of this model is that constructing a 3D crystal with the complex characteristics displayed by the natural sample is less straightforward than with the 2D model.

A general crystal morphology (i.e. type of forms/faces) and aspect ratio were taken following the archetype crystal commonly described in the literature (Faure et al., 2003, 2007; Faure and Schiano, 2004; Welsch et al., 2013, 2014). The aspect ratio of the 3D crystal was chosen based on the *a-c* aspect ratio displayed in the 2D maps (see Figure DR2 for example), and the

dimension along b was chosen to maintain the b - c aspect ratio displayed in Welsch et al. (2013). This yielded a 3D a : b : c aspect ratio of 1.3:0.6:1 respectively, producing a crystal elongated along the a direction (Figure DR3A and DR3B). Once the general morphology of the 3D model was chosen, the more complex framework of the crystal was constructed by (1) first generating the high Fo core (Figure DR3A), (2) creating a hopper crystal (i.e. replicating a disconnected core and rim, Figure DR3B), and (3) building a skeleton (Figure DR3C, also see Figs. 16 and 18 of Welsch et al. 2013). These three crystal parts were combined to yield an olivine that resembled the natural crystal along the a - c section (Figure DR3D).

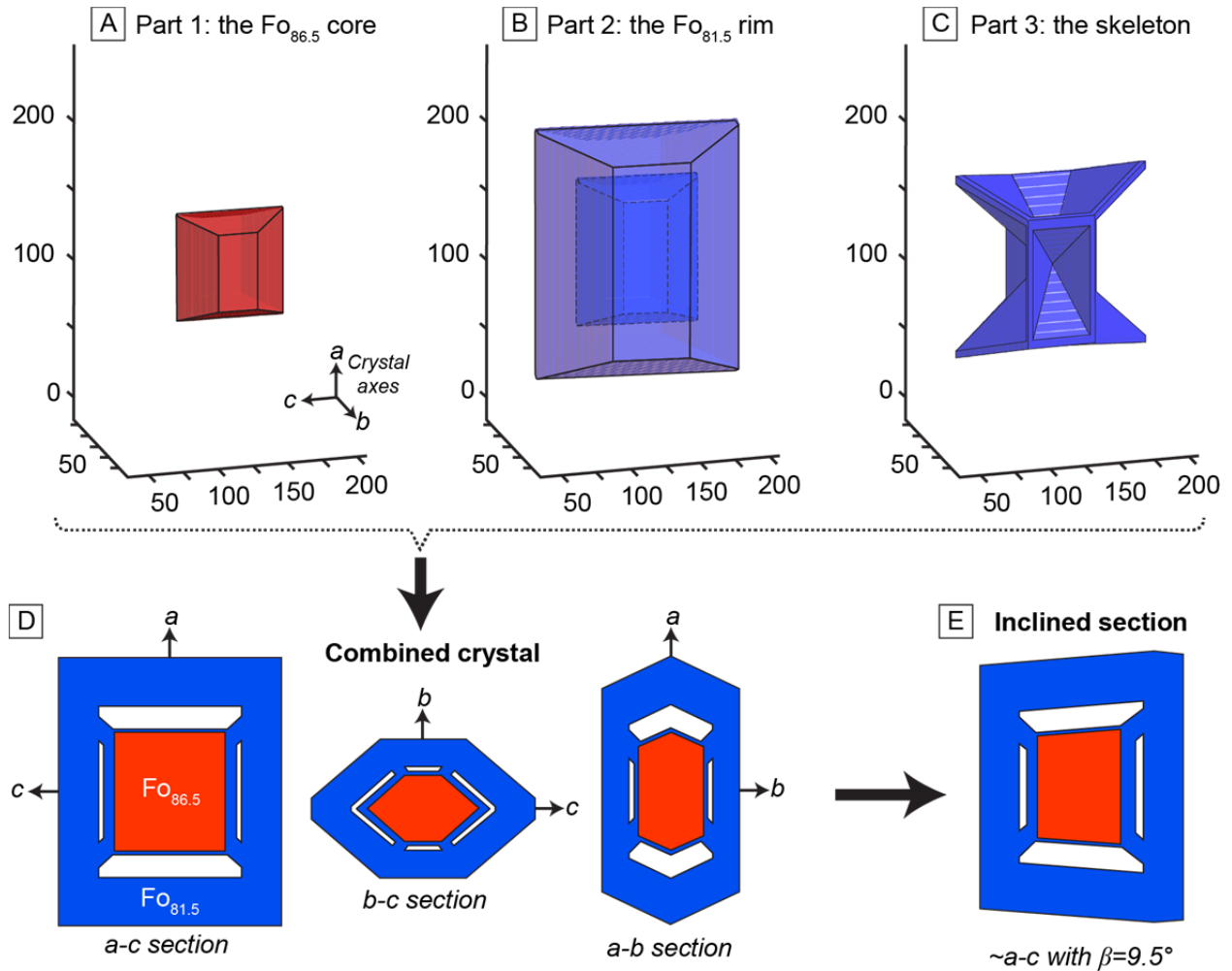


Figure DR3. Procedure for constructing complex 3D crystals. (A) A core and (B) a hopper crystal were built using a typical polyhedral olivine morphology to form the main core-rim assemblage. (C) This assemblage was then connected by a series of 12 spokes radiating from the crystal center, to yield (D) the final crystal assembly, shown here as principal sections through the a - c , b - c and a - b planes. (E) Section slightly oblique to a - c used for comparisons with the calibrated Fo map.

The final 3D olivine template was used as the main input for the diffusion model, which was carried out using methods similar to those for the 2D model, except that the total grid needed

to be reduced to a volume $241 \times 241 \times 241$ (with $4 \mu\text{m}$ per pixel) to allow for reasonable 3D computational times. As diffusion progressed, the best matching 3D model was found by minimizing the difference (i.e. using the Mean Square Root Deviation, e.g. Shea et al. in press) between the concentration gradient measured by EPMA along the c -direction, and a transect taken at the same location in the model (see Figure 1 in the main text for location, and Figure DR4 for the best-matching concentration profile).

COMPARISON BETWEEN 2D, 3D MODELS AND THE NATURAL OLIVINE

The paragraphs above outlined the main methods used to compare the models and the data acquired by EPMA. The concentration profile taken along the c - direction (cf. Fig. 1 in the main text for location), is shown below for the three sets of data (Figure DR4).

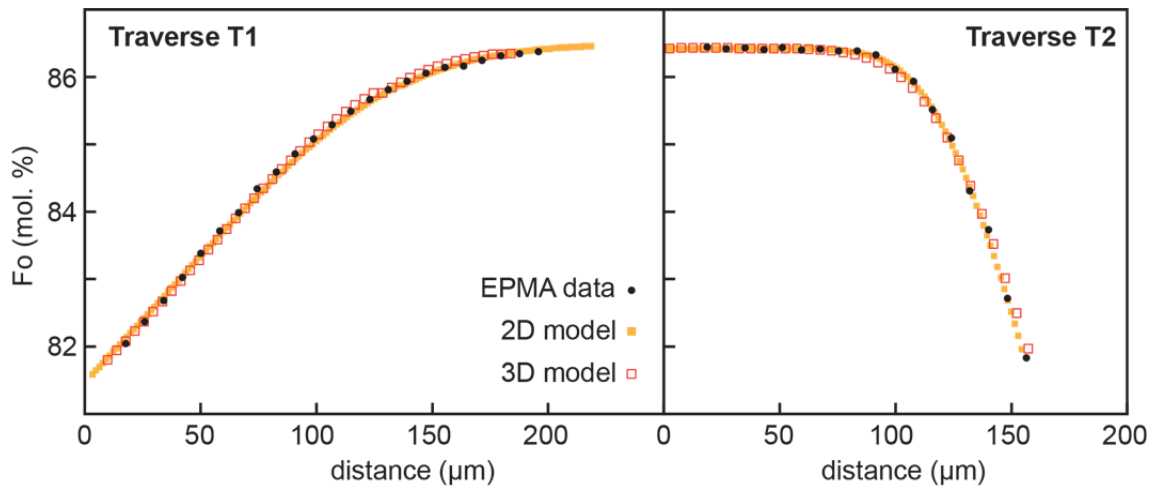


Figure DR4. Comparison between concentration profiles collected by microprobe analyses (see Methods 1 section above), and traverses collected at the same locations T1 and T2 in the 2D and 3D model (Fig. 1B, C and D in main text). The average Fo difference between the ground-truth EPMA data and the 2D and 3D models is in both cases $<0.03\%$ relative

It should be noted that contrary to predictions made in previous studies (e.g., Costa and Chakraborty 2004), the 3D model takes slightly longer than the 2D model to reach a similar final concentration profile (160 and 135 days respectively). Shea et al. (2015) recently revised these predictions to show that 2D-derived timescales can also be longer than 3D times depending on the zoning style (simple normal reverse vs. core-rim zoning), the presence/absence of diffusion anisotropy, and whether the initial core composition is affected or not. Regardless of these added

complexities, the 2D and 3D times only differ by about 15% and lead to the same conclusion about crystal residence time.

FE-MG ZONING DURING RAPID OLIVINE GROWTH: NEVER PRESENT OR NOT PRESERVED?

A classical view is that olivines produced by crystallization of basaltic magmas can be normally-zoned due to concomitant compositional changes of the magma (i.e. progressively more Mg-poor) (e.g. Pearce, 1987). This scenario assumes that olivines grow slowly enough for changes in magma composition to occur, and that crystallization progresses under interface-limited conditions, producing concentrically-zoned crystals. If, as suggested by Welsch et al., (2013, 2014) and by our study, olivine growth is often initially rapid and diffusion-limited (i.e. diffusion in the melt), boundary layers enriched in incompatible elements (e.g. Al, P) and depleted in compatible elements (Fe, Mg) may form around the growing crystal (Faure and Schiano 2005; Hammer 2008; Milman-Barris et al. 2008). In this section, we test two hypotheses for the presence of P zoning and the lack of strong growth-induced Fe-Mg zoning in olivines (see Figure DR5): (1) diffusion of Fe-Mg in the melt is fast enough to erase any boundary layers that are forming around the crystal while slower P diffusion causes built-up and entrapment as ‘solute’ impurities, or (2) diffusion is not fast enough for either P or Fe-Mg and the growing olivine is zoned in both components but only P escapes homogenization via diffusive re-equilibration.

Because Mg is about 3 times more compatible in olivine than Fe (i.e. at conditions relevant to a Kilauea magma crystallizing Fo_{81.5} olivine, the partition coefficients $K_{Mg}^{ol-melt} \approx 5.7$ and $K_{Fe}^{ol-melt} \approx 1.9$, e.g. Beattie, 1993; Matzen et al., 2011), boundary layers will be depleted in the Fo component (i.e. more depleted in Mg than Fe compared to a near-equilibrium scenario). Because P is generally incompatible in olivine in basalt (Milman-Barris et al. 2008; Grant and Kohn 2013), boundary layers will be enriched in phosphorus. For compatible and incompatible elements, Watson and Müller (2009) give expressions to estimate the ‘disequilibrium’ concentration of an element i in a growing crystal surrounded by such boundary layers:

$$C_i^{ol}(diseq.) = \frac{C_i^{ol}(eq.)}{1 - \left(1 - K_i^{ol-melt}\right) \frac{G}{D_i^{melt}} BL} \quad (\text{Incompatible elements})$$

$$C_i^{ol}(diseq.) = \frac{C_i^{ol}(eq.)}{\left(K_i^{ol-melt} - 1\right) \frac{G}{D_i^{melt}} BL + 1} \quad (\text{Compatible elements})$$

Where $C_i^{ol}(eq.)$ is the equilibrium concentration calculated from the distribution coefficient $K_i^{ol-melt}$, G is the crystal growth rate, D_i^{melt} the diffusivity of i in the melt, and BL is the thickness of the boundary layer. At 1200°C, Fe or Mg diffusivity in the melt $D_{Fe/Mg}^{melt} \sim 0.5-1 \times 10^{-11} \text{ m}^2/\text{s}$ (Zhang et al., 2010), and P diffusivity is about half to one order of magnitude lower than for Fe-Mg ($D_P^{melt} \sim 1-3 \times 10^{-12} \text{ m}^2/\text{s}$) using the empirical model of Mungall (2002) or the expression of Watson et al. (in press) extended to lower temperatures. Using crystal growth rates between 10^{-10} (slow) and 10^{-7} m/s (fast), a boundary layer 10-60 μm , and equilibrium compositions $\text{Fo}_{81.5}$ and $\text{P}_2\text{O}_5=0.01 \text{ wt. \%}$ (e.g. Milman-Barris et al. 2008), we calculate the ‘disequilibrium’ composition of a rapidly growing olivine (Fig. DR6).

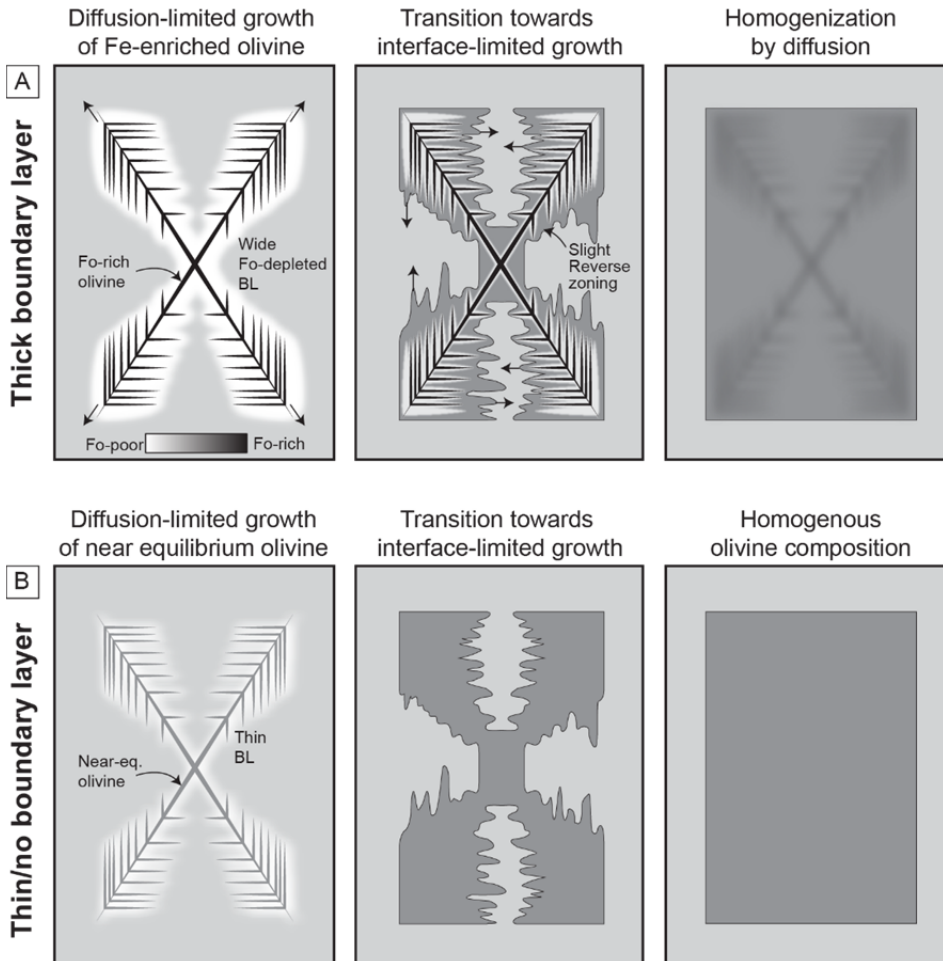


Figure DR5. The effects of rapid crystal growth on Fe-Mg zoning patterns in olivine. A given volume of melt becomes supersaturated in olivine and rapid, skeletal growth ensues. (A) If growth is much faster than diffusion, boundary-layers very depleted in the most compatible element (Mg) and less depleted in other elements (Fe) are generated. The composition of the forming olivine is therefore less forsteritic than it would be at equilibrium. As growth slows down, addition of components to the interface is the limiting factor and olivine composition shifts towards equilibrium, thus potentially generating a slight reverse zoning. Later, Fe-Mg diffusion may erase this type of intricate reverse zoning rapidly. (B) Similar scenario but with much thinner boundary layers, where diffusion of Fe-Mg can nearly keep pace with rapid growth. Near-equilibrium olivine grows and results in very little or no zoning in Fe-Mg.

To compare the model and the natural data, a P enrichment factor was calculated by dividing the intensity of phosphorus in the enriched portions of the olivine by the intensity of P in the ‘normal’ P-poorer zones (enrichment factors between 1.5 and 2). For both Fo and P, the resulting disequilibrium olivine composition curves show that only at very fast growth rates $>10^{-8} \text{ m s}^{-1}$ do significant departures from equilibrium occur for both Fe-Mg and P (Fig. DR6). The difference in diffusivities between these elements in the boundary layer surrounding the olivine is not sufficient to explain the presence of P enrichments coupled with the absence of strong Fe-Mg zoning inferred in our study during each growth stage. Therefore, both Fo and P components should be zoned during rapid growth of olivine, and the lack of preservation of the former would indicate rapid homogenization of Fo during/after crystallization. This analysis is however strongly dependent on both diffusivities of Fe-Mg and P in the melt and crystal growth rates, which are poorly constrained at present. As a result, the two models are maintained in the main text.

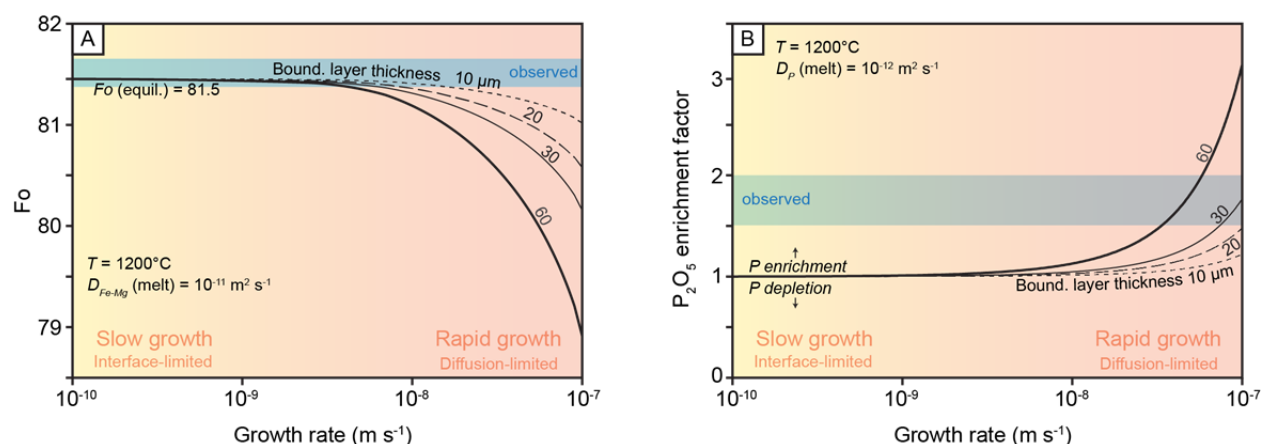


Figure DR6. (A) Fo and (B) P₂O₅ changes in a growing olivine as a function of growth rate and boundary layer thickness. The P enrichment is expressed as the ratio of the disequilibrium P₂O₅ over the inferred equilibrium concentration (P₂O₅(eq.)=0.01 wt.%). In both plots the observed Fo and observed P enrichment factor are displayed as blue regions.

IS THE SKELETAL OLIVINE FROM KILAUEA UNIQUE?

The Kilauea olivine selected for this study is exceptional in that it combines (1) a near-perfect skeletal morphology with an ideal section orientation (close to the a-c plane) and (2) a multi-stage growth history (note: if not, there would not be core-rim compositional differences to measure diffusive re-equilibration with) to unequivocally differentiate zoning patterns produced by growth and diffusion. Because this type of section is particular, an important question is

whether our selected olivine is an isolated occurrence in nature. Although more careful observations are required to answer this question with certainty, we do not believe that this olivine is an isolated case. Skeletal olivine phenocrysts are very common in the products of mafic to intermediate magmas (e.g. New Zealand Arc andesites, Donoghue et al. 1991; Reunion & Hawaii basalts, Welsch et al. 2013, 2014; Stromboli Arc Basalt, Métrich et al. 2010; Apollo Lunar Basalts, Donaldson 1976; Lau Basin Boninites, Glancy 2014), but are rarely examined for zoning compared to euhedral crystals. A recent study of mid-ocean ridge basalts from the Galapagos Spreading Center also found olivine with similarly complex morphology and Fe-Mg zoning patterns (i.e., skeletal with concentric major element zoning at the core, Fig. DR7) (Colman 2014).

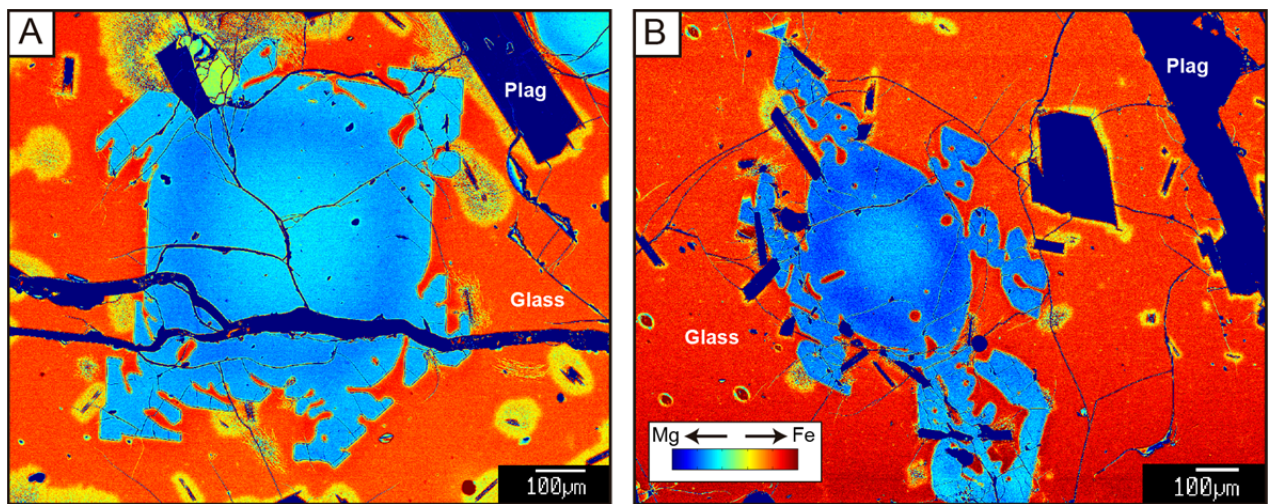


Figure DR7. Olivine crystals in Galapagos MORBs combining skeletal morphologies with complex (reverse followed by normal) zoning (samples from Colman (2014)). These backscatter images were falsely colored (scale on the right) to better highlight compositional differences controlled by Fe-Mg variations (note: scale only valid in olivine). These olivines may have had a multi-stage growth and diffusive re-equilibration history akin to that presented in the main text for the Kilauea example.

Thus, the Kilauea olivine is probably only special in that it was randomly sectioned along an ideal direction to resolve growth vs. diffusion processes (i.e. the high Mg diffusion fingers); other occurrences are probably common in magmas containing skeletal olivine, and, provided more attention is given to their zoning patterns, the conclusions presented in the main text likely have applications to other magma systems.

REFERENCES CITED

- Beattie, P., 1993, Olivine-melt and orthopyroxene-melt equilibria. *Contributions to Mineralogy and Petrology*, v. 115, p. 103-111.
- Chakraborty, S., 2010, Diffusion coefficients in olivine, wadsleyite, and ringwoodite: Reviews in *Mineralogy and Geochemistry*, v. 72, p. 603–639.
- Colman, A., 2014, Effects of variable magma supply on magma reservoirs and eruption characteristics along the Galápagos spreading center: [PhD Dissertation], Honolulu, University of Hawaii at Manoa.
- Costa, F., Chakraborty, S., 2004, Decadal time gaps between mafic intrusion and silicic eruption obtained from chemical zoning patterns in olivine. *Earth and Planetary Science Letters*, v. 227, p. 517-530.
- Costa, F., Dohmen, R., and Chakraborty, S., 2008, Time scales of magmatic processes from modeling the zoning patterns of crystals: Reviews in *Mineralogy and Geochemistry*, v. 69, p. 545-594.
- Dohmen, R., Becker, H., and Chakraborty, S., 2007, Fe-Mg diffusion in olivine I: Experimental determination between 700 and 1200°C as a function of composition, crystal orientation, and oxygen fugacity: *Physics and Chemistry of Minerals*, v. 34, p. 389–407.
- Donaldson, C. H., 1976, An experimental investigation of olivine morphology: *Contributions to Mineralogy and Petrology*, v. 57, p. 187-213.
- Donoghue, S.L., Stewart, R.B., Palmer, A.S., 1991, Morphology and chemistry of olivine phenocrysts of Mangamate Tephra, Tongariro Volcanic Centre" New Zealand. *Journal of the Royal Society of New Zealand*, v. 21, p. 225-236.
- Faure, F., Trolliard, G., Nicollet, C., Montel, J.-M., 2003, A developmental model of olivine morphology as a function of the cooling rate and the degree of undercooling: *Contributions to Mineralogy and Petrology*, v. 145, p. 251–263.
- Faure, F., and Schiano, P., 2004, Crystal morphologies in pillow basalts: implications for mid-ocean ridge processes: *Earth and Planetary Science Letters*, v. 220, p. 331–344.
- Faure, F., Schiano, P., 2005, Experimental investigation of equilibration conditions during forsterite growth and melt inclusion formation: *Earth and Planetary Science Letters*, v. 236, p. 882–898.

- Faure, F., Schiano, P., Trolliard, G., Nicollet, C., and Soulestin, B., 2007, Textural evolution of polyhedral olivine experiencing rapid cooling rates: Contributions to Mineralogy and Petrology, v. 153, p. 405–416.
- Glancy, S.E, 2014, Petrology and Geochemistry of Boninites and Related Lavas from the Mata Volcanoes, NE Lau Basin. [MSc Thesis], Honolulu, University of Hawaii at Manoa.
- Grant, T.B., Kohn, S.C., 2013, Phosphorus partitioning between olivine and melt: An experimental study in the system $\text{Mg}_2\text{SiO}_4\text{-Ca}_2\text{Al}_2\text{Si}_2\text{O}_9\text{-NaAlSi}_3\text{O}_8\text{-Mg}_3(\text{PO}_4)_2$: American Mineralogist, v. 98, p. 1860-1869.
- Hammer, J.E., 2008, Experimental studies of the kinetics and energetics of magma crystallization: Reviews in Mineralogy and Geochemistry, v. 69, p. 5-59.
- Jarosewich, E., Nelen, J. A., Norberg, J. A., 1980, Reference samples for electron microprobe analysis: Geostandards Newsletter, v. 4, p. 43-47.
- Matzen, A.K., Baker, M.B., Beckett, J.R., and Stolper, E. M., 2011, Fe-Mg partitioning between olivine and high-magnesian melts and the nature of Hawaiian parental liquids: Journal of Petrology, v. 52, p. 1243-1263.
- Metrich N., Bertagnini, A., Di Muro, A., 2010, Conditions of Magma Storage, Degassing and Ascent at Stromboli: New Insights into the Volcano Plumbing System with Inferences on the Eruptive Dynamics. Journal of Petrology, v. 51, p. 603-626.
- Milman-Barris, M.T, Beckett, J.R., Baker, M.B., Hofmann, A.E., Morgan, Z., Crowley, M.R., Vielzeuf, D., and Stolper, E., 2008, Zoning of phosphorus in igneous olivine: Contributions to Mineralogy and Petrology, v. 155, p. 739–765.
- Mungall, J.E., 2002, Empirical models relating viscosity and tracer diffusion in magmatic silicate melts: Geochimica and Cosmochimica Acta, v. 66, p. 125-143.
- Pearce, T.H., 1987, The theory of zoning patterns in magmatic minerals using olivine as an example: Contributions to Mineralogy and Petrology, v. 97, p. 451–459.
- Shea, T., Costa, F., Krimer, D., and Hammer, J.E., 2015, Accuracy of timescales retrieved from diffusion modeling in olivine: a 3D perspective: American Mineralogist, in press, <http://dx.doi.org/10.2138/am-2015-5163>.
- Watson, E. B., and Müller, T., 2009, Non-equilibrium isotopic and elemental fractionation during diffusion-controlled crystal growth under static and dynamic conditions: Chemical Geology, v. 267, p. 111–124.

- Watson, E.B., Cherniak, D.J., and Holycross, M.E., 2015, Diffusion of phosphorus in olivine and molten basalt: *American Mineralogist*, in press.
- Welsch, B., Faure, F., Famin, V., Baronnet, A., and Bachelery, P., 2013, Dendritic crystallization: a single process for all the textures of olivine in basalts? *Journal of Petrology*, v. 54, p. 539–574.
- Welsch, B., Hammer, J.E., and Hellebrand, E., 2014, Phosphorus zoning reveals dendritic architecture of olivine: *Geology*, v. 42, p. 867–870.
- Zhang Y., Ni H. and Chen Y., 2010, Diffusion data in silicate melts: *Reviews in Mineralogy and Geochemistry*, v. 72, p. 311–408.